

See discussions, stats, and author profiles for this publication at: <https://www.researchgate.net/publication/231627158>

# Structural Trends among Ionic Metal–Halide Adlayers on Electrode Surfaces

ARTICLE *in* THE JOURNAL OF PHYSICAL CHEMISTRY B · JULY 2000

Impact Factor: 3.3 · DOI: 10.1021/jp000759x

---

CITATIONS

12

---

READS

10

4 AUTHORS, INCLUDING:



Jia Wang

Brookhaven National Laboratory

106 PUBLICATIONS 4,754 CITATIONS

SEE PROFILE

## Structural Trends among Ionic Metal-Halide Adlayers on Electrode Surfaces

J. X. Wang,<sup>\*,†</sup> I. K. Robinson,<sup>‡</sup> J. E. DeVilbiss,<sup>‡</sup> and R. R. Adžić<sup>†</sup>*Materials and Chemical Science Division, Department of Applied Science, Building 555, Brookhaven National Laboratory, Upton, New York 11973, Department of Physics, University of Illinois at Urbana-Champaign, 1110 W Green Street, Urbana, Illinois 61801**Received: February 29, 2000; In Final Form: June 6, 2000*

X-ray diffraction techniques have been used to determine the structures of Tl–Cl, Tl–I, and Pb–Br compounds adsorbed on Au(111) in acid solution. As in the previous case of Tl–Br, several well-defined mixed adlayer phases with stoichiometries of 1:1, 1:2, and 1:3 have been found over a wide potential region. Sufficient data have been gathered to explore the general structural trends among electrochemically prepared two-dimensional (2D) binary ionic compounds. The observed structural phase behavior is rationalized by symmetry and electrostatic considerations in 2D binary ionic crystals. For the 1:1 stoichiometry, square symmetry is generally preferred because it allows an ion to surround itself with the maximum number of counterions. On a hexagonal substrate, this becomes distorted to either a rectangle or a rhombus in commensurate or uniaxially commensurate phases, depending on whether the cation and anion layers are in the same plane.

## Introduction

Structural phase behavior of an adlayer can often be understood in terms of specific environmental effects on an ideal or free-standing two-dimensional (2D) lattice. For example, underpotentially deposited Tl forms a rotated hexagonal monolayer on the least corrugated (111) surfaces of Ag and Au<sup>1–3</sup> because hexagonal symmetry allows a neutral adatom to have the maximum number of near neighbors. On more corrugated (100) surfaces, Tl forms a  $c(p \times 2)$  uniaxially commensurate monolayer, where the hexagonal symmetry is slightly distorted so that all the adatoms can reside between the substrate rows to reduce the buckling of the adlayer.<sup>4</sup> Using this line of thinking, one may ask what are the ideal 2D ionic lattices and how can the phase behavior of the charged adsorbates be understood in terms of the interactions involved? The answers to these fundamental questions can enhance our microscopic understanding of many important interfaces where charged species are involved.

Compared with neutral adsorbate systems, much less is known about the structural phase behavior of ionic adlayers. This is partially due to the lack of suitable experimental methods for producing and studying them. Anion coadsorption with an underpotentially deposited metal monolayer on electrode surfaces has been known for many years. In most cases, coadsorbed anions were found on the top of the metal adlayer and played a secondary role in the adlayer structural behavior.<sup>5–12</sup> Our recent study of Tl–Br coadsorption on the Au(111) electrode surface revealed the formation of three mixed adlayer phases. These phases form at different potentials between the potential of the pure Tl adlayer and the potential of the pure Br adlayer (see Figure 1).<sup>13</sup> In the  $(3 \times \sqrt{3})$ -2TlBr and  $(\sqrt{13} \times \sqrt{13})$ -3TlBr<sub>2</sub> phases, both Tl and Br are found in the first adlayer with spacings close to that in bulk TlBr crystal. These demonstrate that a well-ordered 2D ionic crystal can be made

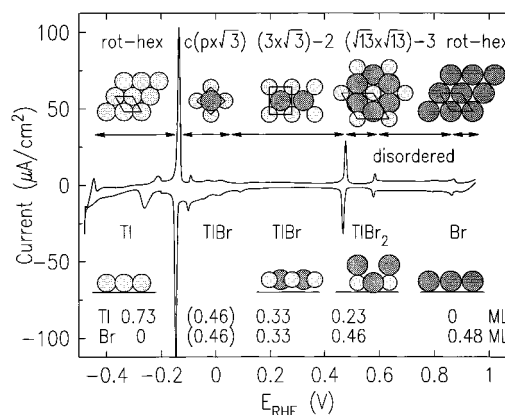


**Figure 1.** Voltammetry curve for Tl–Br coadsorption on Au(111) in 0.1 M HClO<sub>4</sub> containing 1 mM TlBr. Sweep rate, 20 mV/s. The in-plane and surface normal structural models are deduced from the surface X-ray diffraction measurements.<sup>13</sup> Coverages are given in units of monolayers (ML) of the Au substrate and are calculated from the adlayer lattice constants. In the pure Tl and Br phase, coverages change slightly with potential. The  $c(p \times \sqrt{3})$  phase is weakly ordered, that is, only small patches exist and the average coverage over a large area may be smaller than that shown.

by electrosorption when a suitable metal-anion/substrate system is chosen. Because the partial charge and adsorption strength of the adions tend to vary continuously with potential, the structures that actually form and lock over a certain potential region show what structures are the most favorable for 2D ionic compounds.

To identify the basic types of binary ionic adlayers, we begin by considering the high-symmetry arrangements in free-standing 2D ionic crystals because they are often favored over lower symmetries. In Figure 2, a typical binary ionic system is modeled by two kinds of spheres close in size and carrying opposite charges. For such a system to belong to a high-symmetry plane group, not only the unit cell but also the arrangements of the components in the unit cell need to be considered. Therefore, only certain stoichiometries can be accommodated as illustrated.

\* Corresponding author. E-mail jia@bnl.gov.

<sup>†</sup> Brookhaven National Laboratory.

<sup>‡</sup> University of Illinois at Urbana-Champaign.

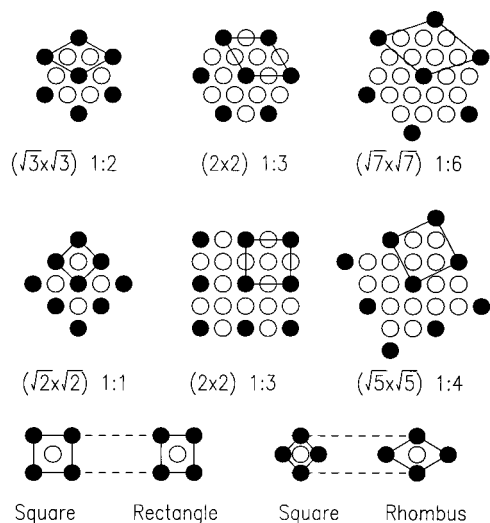


**Figure 2.** Low-order allowed stoichiometries for binary ionic 2D crystals with hexagonal (top) and square (middle) symmetries. A square lattice can be distorted by contraction or expansion along one side or one diagonal direction, resulting in either a rectangle or rhombus (bottom). The open and filled circles represent ions A and B, which carry opposite charges.

In hexagonal lattices, the unit cells with hexagonal symmetry are found by sequentially increasing the hexagonal lattice constant from unity (with respect to the nearest neighbor spacing) to  $\sqrt{3}$ , to 2, and to  $\sqrt{7}$ , etc. In the  $(\sqrt{3} \times \sqrt{3})$ ,  $(2 \times 2)$ , and  $(\sqrt{7} \times \sqrt{7})$  unit cells, the 6-fold rotational symmetry holds only when the stoichiometries are 1:2, 1:3, and 1:6, respectively. It also becomes clear that the hexagonal symmetry is not possible for the 2:3, 1:4, and 1:5 stoichiometries. By using the same approach for a square lattice, as shown in the middle panel of Figure 2, one finds that the 1:1, 1:3, and 1:4 stoichiometries can contain a 4-fold rotation axis, but not the 1:2. Although many more stoichiometries having 6- or 4-fold rotational symmetry can be found by further increasing the size of the unit cell, the mirror symmetry is restricted to the first two cases for both hexagonal and square lattices. Therefore, the 1:2 and 1:3 hexagonal and the 1:1 and 1:3 square lattices should be the most favorable for a free-standing 2D binary ionic crystal.

On a single-crystal substrate surface, adlayers often form commensurate or uniaxially commensurate structures to reduce the buckling at the expense of a symmetry distortion from ideal 2D lattices. As illustrated in the bottom part of Figure 2, distortions of a 1:1 square can result in either a rectangle or a rhombus. The lattice spacing along one side or one of the diagonal directions is constrained by the substrate, whereas the other contracts or expands appropriately. Examples are the  $(3 \times \sqrt{3})$ -2TlBr and  $c(p \times \sqrt{3})$ -TlBr phases (Figure 1), where the primitive unit cells, respectively, have one side and one diagonal spacing being  $\sqrt{3}$  of the Au(111) lattice spacing. These structures are preferred because the buckling of the adlayer declines when the atop sites can be avoided. Thus, on hexagonally close-packed substrates, the basic types of binary ionic adlayer lattices are likely to be the 1:1 rectangle, 1:1 rhombus, and the 1:2 and 1:3 hexagons. The notation “hexagon” is used in this article to mark the high symmetry of a hexagonal lattice where the unit cell is a rhombus with an exact  $120^\circ$  angle between the two lattice vectors. And, as a special case of rhombus, a hexagonal lattice is *included* in the 1:1 rhombus.

The predictions discussed above are examined in this article in light of the results of our surface X-ray scattering (SXS)

studies of metal-halide coadsorption on Au(111). Although SXS is not directly element-sensitive, analysis of diffraction intensities can provide reliable determination of mixed adlayer structure if the electron densities are significantly different between the cation and anion. This is the case for the coadsorption of Tl ( $Z = 81$ ) or Pb ( $Z = 82$ ) with Cl ( $Z = 17$ ), Br ( $Z = 35$ ), or I ( $Z = 53$ ). Also, because these ions are similar in size and larger than the substrate atom, their phase behaviors are likely to show the characteristics of a 2D ionic crystal with moderate substrate influence. In the Tl-halide systems, the wide (about 1 V) coadsorption potential region between the two pure phases provides possibilities for the formation of a 2D ionic crystal with, in principle, the whole range of stoichiometry. All four basic types of lattices (the 1:1 rhombus and rectangle, and the 1:2 and 1:3 hexagons) have been found. For the Pb-Br coadsorption on Au(111), detailed analysis revealed the centered-rhombic symmetry for the 1:1 coadsorbed bilayers. This is contradictory to the structure constructed by taking two layers from bulk crystals, indicating the need for a fundamental understanding of 2D ionic crystals.

Historically, one of the earliest applications of X-ray diffraction was the discovery of the principles of ionic radius in ionic crystals, described by Pauling.<sup>14</sup> With the availability of data on several *two-dimensional* ionic compounds, including those reported here, those principles can be extended to surface and interface situations. To cite a simple example of the relevant considerations that influence structural trends in bulk ionic crystals, we consider the well-studied alkali halides. These alkali halides may adopt either the sodium chloride (NaCl) or cesium chloride (CsCl) lattices but sometimes show phase transitions between these structures.<sup>15</sup> The structural principle involved here is a competition between  $1/r^2$  electrostatic attraction of the ions and a  $1/r^n$  hard-sphere repulsion between the ion cores.<sup>16</sup> Because it is longer range, the electrostatic attraction contribution dominates the energy at the equilibrium interionic spacing, which is given by the sum of “univalent radii”.<sup>14</sup> To explain the observed nearest-neighbor spacings in crystal structures, several small corrections are needed to account for “double repulsion” and for the variation of the potential with ionic coordination.<sup>17</sup>

## Experimental Section

The Au(111) crystal (miscut  $< 0.2^\circ$ ) was annealed in a propane flame before each experiment.<sup>18</sup> To prevent contamination from the air, a drop of water was put onto the surface when the crystal cooled to  $\sim 100^\circ\text{C}$  and was kept there during the transfer to the X-ray electrochemical cell.<sup>19</sup> After each experiment, the Au(111) crystal was immersed in concentrated  $\text{HNO}_3$  for at least a half-hour to ensure complete removal of metal adsorbates. Observations related to duration of the experiment or potential cycling history were reproducible using this cleaning procedure. The solutions were prepared from  $\text{Ti}_2\text{CO}_3$ , PbO, KCl, KBr, KI salts (Aldrich),  $\text{HClO}_4$  acid (Merck), and Millipore QC UV Plus water (Millipore Inc.). Potentials were measured relative to either a Ag/AgCl (3 M NaCl) electrode or a reversible hydrogen electrode (RHE). An outer chamber was filled with high-purity nitrogen gas to prevent oxygen diffusing through the X-ray window during the measurements. For the Tl-I system, because of its low solubility, the cell was inflated for each potential change to eliminate the variation of local concentration in the thin solution layer above the crystal.

X-ray measurements were performed at the beam line  $\times 22\text{A}$  with  $\lambda = 1.20 \text{ \AA}$  at the National Synchrotron Light Source. A four-circle diffractometer was used in the symmetric  $\omega = 0$

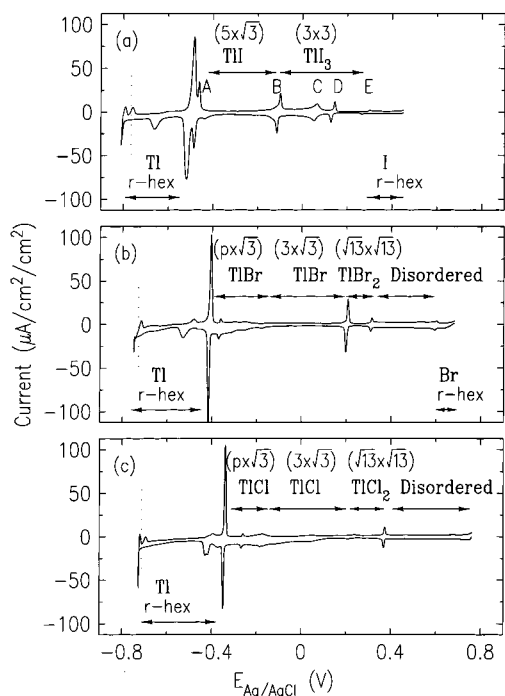


**Figure 3.** Voltammetry curves obtained from a hanging meniscus Au-(111) electrode in 0.1 M  $\text{HClO}_4$  solution containing 0.2 mM TlI (a), 1 mM TlBr (b), and 2 mM TlCl (c). Sweep rate, 20 mV/s. The dotted lines mark the Nernst potential of Tl bulk deposition calculated for the corresponding  $\text{Tl}^+$  concentration.

mode.<sup>20</sup> Following convention, a hexagonal coordinate system was used for the substrate crystal in which the reciprocal-space wave vector was  $Q = |H\bar{a}^* + Kb^* + Lc^*|$ , where  $a^* = b^* = 4\pi/\sqrt{3}a$ ,  $c^* = 2\pi/\sqrt{6}a$ ,  $a = 2.885 \text{ \AA}$ , and  $L$  is along the surface normal direction.<sup>19</sup> Most in-plane measurements were conducted at  $L = 0.2$ , and the peak positions are indexed by  $(H, K)$ . Soller slits were used for getting the best signal-to-background ratio in monitoring the phase transition during potential scans and in searching diffraction signals in the disordered phases. All the integrated intensities, however, were measured with a 2-mm vertical slit and a 2- or 4-mm horizontal slit located 650 mm from the sample. The resulting resolution in the surface plane is larger than the intrinsic peak width for all measured reflections. The structure factors were obtained after correcting the integrated intensities for the variation of the Lorentz factor, the effective sample area, and the resolution along the surface normal direction.<sup>21</sup>

## Results and Discussions

**Tl-I, Br, Cl/Au(111).** The voltammetry curves for Au(111) in 0.1 M  $\text{HClO}_4$  solution containing TlI, TlBr, and TlCl are shown in Figure 3, with the potential regions of ordered phases indicated. Different concentrations have been used because the same high concentration of solutes, desirable for minimizing diffusion-controlled processes, could not be achieved for TlI and TlBr because of their low solubilities. In all three solutions, a pure Tl monolayer exists between the Nernst potential (dotted vertical lines) and the potential of the largest current peak. This potential region apparently decreases in the order  $\text{Cl} > \text{Br} > \text{I}$  because of the increasing anion adsorption strength from Cl to Br to I. In TlCl solution, except for the potential range, structures of the three Tl-Cl adlayer phases are similar to those of Tl-Br reported earlier.<sup>13</sup> For the uniaxially incommensurate  $c(p \times \sqrt{3})-2\text{TlCl}$  phase,  $p$  is 2.10, slightly smaller than the value of 2.14 for Tl-Br. The two commensurate phases,  $(3 \times$

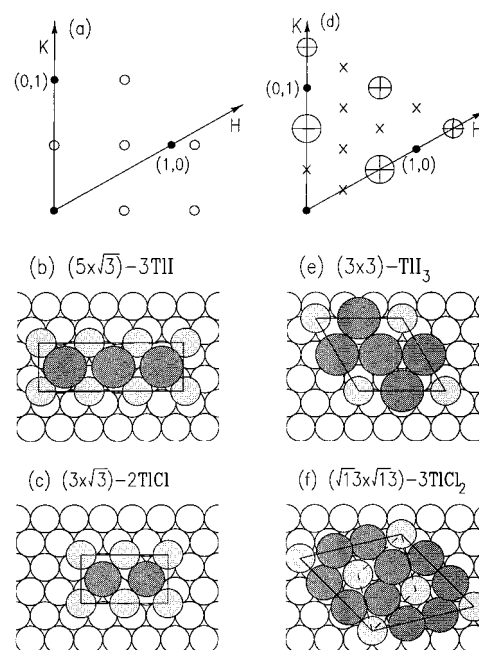


**Figure 4.** Structural models for Tl-I mixed adlayers (b and e) are deduced from observed diffraction patterns shown by the open circles in a and d, respectively. Similar structures observed from TlCl solutions are shown in c and f for comparison. The diameters of the open, lightly shaded, and heavily shaded circles represent the relative sizes of Au atoms (2.885  $\text{\AA}$ ),  $\text{Tl}^+$  (2.98  $\text{\AA}$ ), and  $\text{I}^-$  (4.30  $\text{\AA}$ ) or  $\text{Cl}^-$  (3.62  $\text{\AA}$ ) ions, respectively. The areas of the open circles in d represent the measured structure factor intensity, whereas the size of the plus signs show the calculated values based on the TlI<sub>3</sub> model shown in e. All other allowed diffraction peaks that have not been observed are shown by "X" and their calculated intensities are less than 2% of the  $(2/3, 2/3)$  peak.

$\sqrt{3})-2\text{TlCl}$  and  $(\sqrt{13} \times \sqrt{13})-3\text{TlCl}_2$ , are determined by analysis of the in-plane structural factor intensities. (See Appendix for details.) Specular reflectivity obtained for the  $(3 \times \sqrt{3})-2\text{TlCl}$  phase confirms the  $1/3$  monolayer coverage and yields the information along the surface normal direction. The layer spacings of Cl and Tl from the top layer of the Au(111) surface are 2.55 and 2.80  $\text{\AA}$ , respectively. Extensive searching did not find any ordered phase at potentials positive of 0.4 V. Iodide and bromide differ considerably in adsorption strength, charge transfer, and size. Consequently, larger differences in lattice structures are observed. A detailed structure determination is given below for Tl-I. The results are compared with those for Tl-Cl and Tl-Br.

The SXS measurements for TlI started at  $-0.7 \text{ V}$ , slightly positive of the bulk deposition potential. Diffraction peaks corresponding to a rotated-hexagonal Tl monolayer were observed. As the potential increased, the diffraction intensity from the Tl monolayer started to decrease at  $-0.55 \text{ V}$  and vanished at  $-0.4 \text{ V}$ . The potential-dependent lattice constant and rotation angle have the same behavior as in the absence of iodide,<sup>2</sup> indicating little effect of iodide at potentials negative of  $-0.5 \text{ V}$ .

At the potentials between the current peaks A ( $-0.43 \text{ V}$ ) and B ( $-0.12 \text{ V}$ ), a new set of fractional diffraction peaks was observed. These can be indexed by the basis vectors of  $(0.6, -0.3)$  and  $(0, 0.5)$  for one of the three symmetry equivalent domains, as shown in Figure 4a. The corresponding  $(5 \times \sqrt{3})-3\text{TlI}$  real space lattice is shown in Figure 4b. The  $\theta$ -rocking curves through the three lowest order diffraction peaks, indexed with respect to the rectangular adlayer lattice, are shown by the solid lines in Figure 5. A larger  $\theta$ -angle



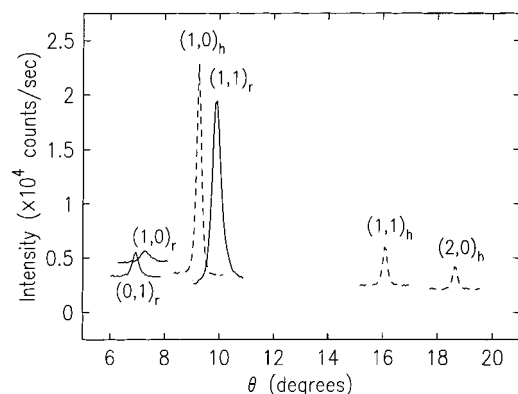


**Figure 5.** In-plane  $\theta$ -rocking scans at  $L = 0.25$  through the peaks for the rectangular TII (solid lines) and the hexagonal  $\text{TI}_3$  (dashed lines) adlayers. The peaks are indexed by the adlayer lattice. Thus,  $(10)_r$  and  $(01)_r$  correspond to the first-order diffraction at  $(0.6, -0.3)$  and  $(0, 0.5)$  for the rectangular  $(5 \times \sqrt{3})$ -TII adlayer and  $(10)_h$  and  $(01)_h$  corresponds to the first-order peak at  $(2/3, 0)$  and  $(0, 2/3)$  for the hexagonal  $(3 \times 3)$ - $\text{TI}_3$  adlayer.

represents a larger in-plane momentum transfer. If there was only one atom in the unit cell, increasing the  $\theta$  angle would decrease the integrated intensity from the rocking curve without corrections. Therefore, the fact that the second-order peaks at higher  $\theta$ -angles are more intense than the two first-order peaks clearly indicates that the adlayer has a mixed centered structure. In the proposed model (Figure 4b), I and Tl adions are at the corners and in the center of the  $(1.667 \times \sqrt{3})$  primitive unit cell, respectively. Thus the first- and second-order peaks have structure factors that are the difference and the sum of the form factors of Tl and I, respectively. (See Appendix for details.) This lattice has the same symmetry as the  $(3 \times \sqrt{3})$ - $2\text{TICl}$  phase as shown in Figure 4c. The larger lattice spacing in one direction for TII ( $5/3a = 4.808 \text{ \AA}$ ) compared with TICl ( $3/2a = 4.323 \text{ \AA}$ ) may be attributed to the size difference between the two anions. In both cases, the measured structure factor intensities of the two first-order peaks relative to the strong second-order peak are within 10% of calculated values, confirming the models shown.

Above  $-0.1 \text{ V}$ , near the current peak B, the  $(5 \times \sqrt{3})$ -TII phase vanishes and a mixed  $(3 \times 3)$  adlayer forms, giving rise to the  $(0, 2/3)$ ,  $(2/3, 2/3)$ , and  $(0, 4/3)$  diffraction peaks (dashed lines in Figure 5). These peaks emerge at potentials positive of peak B, and the intensities increase slowly to the maximum value at potentials between peaks D and E. This may be caused by the slow kinetics of the phase formation, which is improved at high potentials. The structure factors of these peaks were measured at  $0.25 \text{ V}$  by integration of the  $\theta$ -rocking curves. The data (areas of the open circles) shown in Figure 4d are in good agreement with the calculated values (the size of the plus signs) for the  $\text{TI}_3$  model (Figure 4e). Because it is difficult to measure the in-plane diffraction intensity on an absolute scale, the relative intensity pattern is obtained by normalizing the data so that the intensity for the first-order peak equals the calculated value. In doing so, the  $\text{TI}_3$  and  $\text{TI}_3\text{I}$  models become indistinguishable by the in-plane data because the intensity distribution patterns happen to be very similar, despite the differences on an absolute scale.

To determine the stoichiometry ( $\text{TI}_3$  or  $\text{TI}_3\text{I}$ ) and the structure along the surface normal direction, specular reflectivity measurements were carried out for the  $(3 \times 3)$  phase. Figure 6 shows the integrated intensities at different  $L$  along the  $(0, 0, L)$  rod, where the normalization factor is obtained by fitting the data near the  $(0, 0, 3)$  Bragg position ( $L$  from 2.8 to 3.2). The data

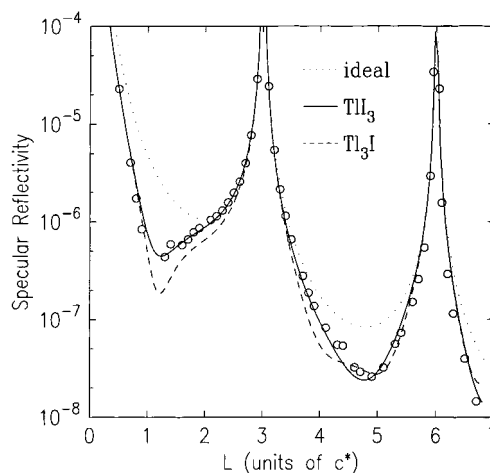


**Figure 6.** Specular reflectivity (circles) measured for Au(111) at  $0.25 \text{ V}$  in  $0.1 \text{ M HClO}_4$  containing  $0.2 \text{ mM TII}$ . The dotted line shows the curve for an ideal Au(111) crystal. The dashed and solid lines are the fits using the models discussed in the text.

(circles) clearly differ from the adsorbate-free Au(111) reflectivity profile (dotted line) and are analyzed using a real space model that incorporates an ideally terminated Au(111) crystal, a nonideal Au top layer, a thallium monolayer, and an iodide monolayer. Each of these three surface layers is described by an atomic coverage normalized to an ideal Au(111) plane, a layer spacing, a vertical root-mean-square (rms) displacement amplitude, and the corresponding atomic form factor. In the fitting, the density of the Au top layer is always fixed at unity and the Tl coverage is held at either  $1/9$  or  $3/9$ , with the I coverage fixed at  $3/9$  or  $1/9$ , respectively. The former corresponds to the  $\text{TI}_3$  model and gives a better fit (solid line, the goodness of fit,<sup>22</sup>  $\chi^2 = 0.11$ ) than the latter which represents the  $\text{TI}_3\text{I}$  model (dashed line,  $\chi^2 = 0.16$ ). For the best fit by using the  $\text{TI}_3$  model, the layer spacings from the Au top layer to the I and Tl adlayers are  $2.58$  and  $3.47 \text{ \AA}$ , respectively. There is essentially no change in the layer spacing for the top gold layer. The rms values are  $0.1 \text{ \AA}$  for the Tl and I adlayers and  $0.15 \text{ \AA}$  for the top gold layer. This hexagonal mixed adlayer disappears at potentials positive of  $0.3 \text{ V}$ , near the current peak E.

At  $0.35 \text{ V}$ , an off-axis diffraction peak is seen at  $(-0.345, 0.758)$  as expected for a rotated-hexagonal pure I adlayer. Both the coverage ( $0.432$  monolayers) and rotation angle ( $3^\circ$  off the  $(11)$  axis) are within the ranges previously observed in the KI solutions.<sup>23</sup> The potential range for this phase is also similar to that in the absence of Tl. These facts suggest no coadsorption of  $\text{TI}^+$  ions at potentials positive of  $0.35 \text{ V}$ . Compared with the onset of Tl coadsorption with Br around  $0.6 \text{ V}$ , Tl coadsorption with I occurs at significantly lower potentials. This difference can be attributed to the lower discharge potential of iodide with respect to bromide and hence shows the ionic nature of metal-halide coadsorption.

Returning the potential to the region below  $0.2 \text{ V}$  regenerates a set of diffraction peaks on the  $(01)$  and  $(11)$  axis. These peaks, however, are shifted from  $(0, 2/3)$  and  $(2/3, 2/3)$  to  $(0, 0.696)$  and  $(0.696, 0.696)$ , respectively. Because the symmetry and stoichiometry are the same as for the  $(3 \times 3)$ - $\text{TI}_3$  adlayer, the peak shift indicates a 4% decrease of lattice spacing (from  $4.32$  to  $4.15 \text{ \AA}$ ) and a 6% increase of coverage (from  $0.11$  to  $0.12$  monolayer of  $\text{TI}_3$ ). The change from a commensurate to an incommensurate hexagonal adlayer appears to be "irreversible", that is, even after cycling the potential down to  $-0.4 \text{ V}$ , the  $\text{TI}_3$  hexagonal phase that reappears at high potentials is still

**TABLE 1: Radii ( $R$ ) and the NNS in the  $(3 \times \sqrt{3})$ -2TlCl,  $(3 \times \sqrt{3})$ -2TlBr, and  $(5 \times \sqrt{3})$ -3TlI Phases**

	Tl	Cl	Br	I
$R_{\text{ion}}^a$	1.49	1.81	1.96	2.20
$R_{\text{bulk}}$ or $R_{\text{vdW}}^a$	1.73	1.81	1.95	2.15
	Tl-Cl	Tl-Br	Tl-I	
NNS in the rectangular phases <sup>b</sup>	3.35	3.38	3.61	
NNS in the bulk crystals <sup>c</sup>	3.33	3.43	3.63	
sum of ionic radii	3.30	3.45	3.69	
sum of bulk and VdW radii	3.54	3.68	3.88	

<sup>a</sup> Emsley.<sup>25</sup> <sup>b</sup> Calculated from the in-plane lattice constants and the layer spacings between Tl and halide. <sup>c</sup> Calculated from the lattice constants of the CsCl type structure.<sup>26,27</sup>

incommensurate. The phase was recovered after the crystal was cleaned and flame-annealed. This behavior may be related to the changes of surface morphology at high potential which do not completely recover after returning to the low potential. This kind of change in surface morphology has been observed by STM on Au in halide-containing solutions.<sup>24</sup>

For all three Tl-halide systems, the ionic nature of the mixed adlayers in the rectangular phase can be ascertained by the following facts. As shown in Table 1, the Tl-Cl, Tl-Br, and Tl-I nearest-neighbor spacings (NNS) in the  $(3 \times \sqrt{3})$ -2TlCl,  $(3 \times \sqrt{3})$ -2TlBr, and  $(5 \times \sqrt{3})$ -3TlI phases are close to both the corresponding values in the bulk Tl-halide ionic crystals and the sum of ionic radii. The ionic radii of halides are essentially the same as the van der Waals radii (because of their filled shell configuration), but this is not so for Tl and Tl<sup>+</sup>. Consequently, the agreements of NNS with the sum of ionic radii in all three cases suggests that the Tl adatoms are at least partially charged. Neutral Tl adatoms are clearly too big to fit in the observed lattices, because the NNS in bulk Tl (3.46 Å) is 16% larger than the diameter of Tl<sup>+</sup> ion (2.89 Å). The quasi-square arrangement in these phases also indicates a strong electrostatic interaction of charged adsorbates. Square symmetry is preferred for 1:1 ionic monolayers because it allows each adion to be surrounded by a maximum number of counterions. Conversely, if the interaction between the two opposite charges is weak or absent, the close-packed monolayers will likely be closer to a hexagonal arrangement because the nearest neighbors can increase from four to six. Two cases have previously been found which show the symmetry change from quasi-hexagonal to quasi-square due to ionic coadsorption. On Au(110), a centered-rectangular lattice has been found for iodide coadsorption with Cs or other alkali-metal cations. In contrast, all three pure iodide phases at higher potential are quasi-hexagonal.<sup>28</sup> On Au(100), the adlayer lattice changes from  $c(\sqrt{2} \times 2\sqrt{2})$  (quasi-hexagonal) to  $c(2 \times 2)$  (square) in bromide-containing solution when the cation species changes from the nonadsorbing Na<sup>+</sup> to tetrabutylammonium which coadsorbs with halides.<sup>29</sup>

The formation of the 1:2 and 1:3 hexagonal lattices and the absence of other structures over the wide potential regions indeed shows that the high-symmetry lattices are most likely to form. The anions in these phases can be in a single or two separated layers, and the lattice can be commensurate or incommensurate. The stoichiometry for well-ordered adlayers, however, appears to be limited to those which allow high-symmetry atomic arrangements as discussed in the Introduction. For metal-rich phases, the 2:1 hexagonal lattice has been found in the underpotential deposition (UPD) of Cu<sup>9</sup> and Hg<sup>30</sup> in sulfuric acid solution. On (100) surfaces, the 1:3 square structure has been reported for KBr<sub>3</sub> on Au(100) based on low-energy

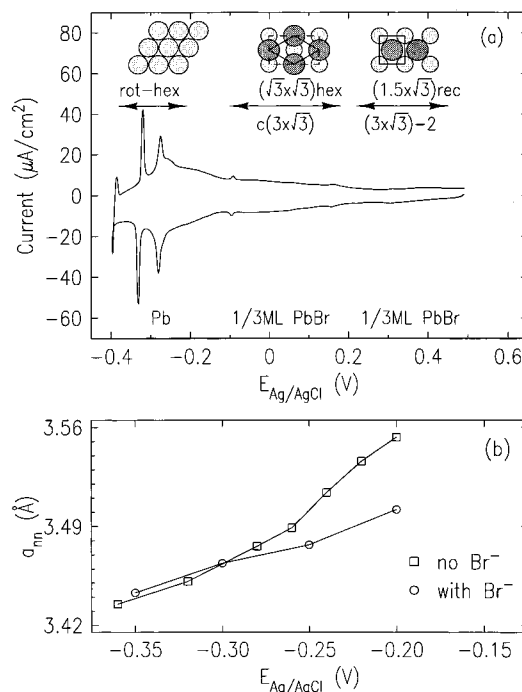


**Figure 7.** (a) Voltammetry curve obtained from a hanging meniscus Au(111) electrode in 0.1 M HClO<sub>4</sub> solution containing 5 mM PbO and 5 mM KBr. Sweep rate, 20 mV/s. Structural models are shown in the potential region of their existence. The light and heavy shaded circles represent Pb and Br, respectively. Coverages shown are calculated from the adlayer lattice constants. (b) The change of the nearest neighbor separation in the rotated-hexagonal Pb monolayer as a function of potential with and without Br<sup>-</sup>.

electron diffraction and electrochemical studies.<sup>31</sup> This structure, however, needs further study, because the suggested Br-Br separation of 1.74 Å seems too small compared with the diameter of Br<sup>-</sup> (3.92 Å).<sup>25</sup>

**Pb-Br/Au(111).** The UPD of lead and thallium, which are next to each other in the periodic table, have several similarities including formation of rotated-hexagonal monolayer prior to bulk deposition.<sup>3</sup> An important difference in their behavior is that Pb has a more positive reversible potential. As shown in Figure 7a, the onset of Pb bulk deposition occurs at -0.39 V on Au(111) in perchloric acid containing 5 mM Pb<sup>2+</sup> and 5 mM Br<sup>-</sup>. This is close to the potential where the unaffected hexagonal Tl monolayer vanishes and coadsorption of Tl and Br begins. In the potential region from -0.38 to -0.2 V, Pb formed an incommensurate hexagonal monolayer which rotates from the Au substrate axis by 9–9.5° depending on the potential. In the absence of Br<sup>-</sup>, we found a significantly smaller rotation angle of 3–3.6°, which is close to the value (2.5°) reported by Toney et al.<sup>3</sup> The potential dependence of the hexagonal lattice spacing is shown in Figure 7b, together with that in the absence of Br<sup>-</sup>. Although similar values are found at the most negative potentials, the lattice spacing increases with increasing potential less rapidly in the presence of bromide. These differences, although small, are reproducible and provide evidence for weak adsorption of Br<sup>-</sup> ions around -0.3 V and its influence on a close-packed metal monolayer.

As shown in Figure 7a, there are two sharp current peaks around -0.3 V over a broad constant current level below -0.1 V. Because there are no discontinuous changes in Pb monolayer structure near -0.3 V and the integrated charges under these peaks are small, these sharp peaks likely result from a capacitance charging in response to the onset of bromide adsorption. The absence of a major current peak near the

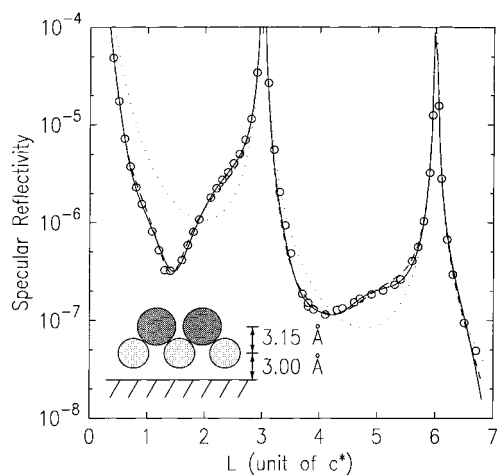


**Figure 8.** Specular reflectivity (circles) obtained at 0.06 V for the PbBr hexagonal phase on Au(111) in the 0.1 M HClO<sub>4</sub> solution containing 5 mM PbO and 5 mM KBr. The dotted line shows the curve for an ideal Au(111) crystal. The dashed and solid lines are the fits using the models discussed in the text.

potential where the hexagonal Pb monolayer vanishes indicates that the change of Pb and Br coverages occurs slowly over a wide potential range. Consequently, the formation of the  $(\sqrt{3} \times \sqrt{3})$ -PbBr phase was rather slow in a positive potential sweep. The maximum in-plane diffraction intensity from the mixed adlayer phase was reached after an hour at 0.05 V. There is also no major current peak near the phase-transition potential between the  $(\sqrt{3} \times \sqrt{3})$  and the  $(3 \times \sqrt{3})$  phases. The explanation seems to be simply that there is no change in coverage between these two phases. We noticed, however, there is a complication related to the kinetics of the initial formation of the centered rectangular  $(3 \times \sqrt{3})$ -2PbBr phase. It appeared only after several positive potential sweeps. Once it formed, however, the phase transition between the two mixed adlayers occurred repeatedly in the potential cycles. This behavior may be related to the slow activation of the substrate lateral relaxation involved in the  $(3 \times \sqrt{3})$ -2PbBr phase. The evidence for the substrate lateral relaxation is the observation of the  $(1/3, 5/6)$  in-plane diffraction peak. Detailed discussion on this peak has been given previously for the  $(3 \times \sqrt{3})$ -2TlBr phase.<sup>13</sup>

Despite the complications in the phase-transition kinetics, SXS data collected from two Au(111) crystals were consistent. The detailed analysis of these data is given below. The 1:1 stoichiometry and Pb-Br layer spacing in the  $(\sqrt{3} \times \sqrt{3})$  phase were determined from analysis of the specular reflectivity profile shown in Figure 8. The layer spacing and the vertical rms displacement amplitude for the Pb and Br adlayers, as well as the top Au layer are allowed to vary. The dotted line shows the calculated curve for an ideal Au(111) crystal, and the dashed line is the fit to the data using the structural model containing 1/3 Pb and 1/3 Br monolayer. Models with either 1/3 Pb and 2/3 Br monolayer or 2/3 Pb and 1/3 Br monolayer fail to produce reasonable fits and hence are ruled out. The fit can be slightly improved (solid line,  $\chi^2$  decreased from 0.023 to 0.015) by allowing the Br coverage to vary in fitting, which leads to a decrease of Br coverage from 0.33 to 0.26 monolayer and the rms width of the Gaussian distribution of Br adlayer from 0.8 to 0.24 Å. The layer spacings, however, do not change significantly and clearly indicate a bilayer structure in which the Pb and Br adlayer are  $3.00 \pm 0.05$  and  $6.15 \pm 0.05$  Å above the Au substrate, respectively.

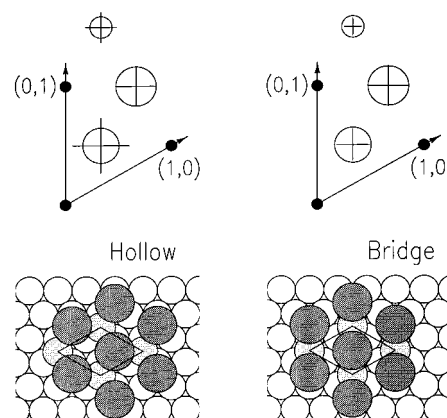


**Figure 9.** Measured in-plane structure factor intensities are shown by the area of the open circles for two sets of symmetry equivalent peaks. The data are compared with calculated values (size of the plus sign) based on the models in which Br (heavily shaded) resides in the hollow (left) and at the bridge (right) site of the Pb (lightly shaded) hexagonal adlayer. In the calculations, contributions from the symmetry equivalent domains are averaged.

Structure factor analysis of the in-plane diffraction peaks has been performed to determine the in-plane position of the Br adion with respect to the underlying hexagonal Pb adlayer. Measured intensities at the  $(1/3, 1/3)$ ,  $(2/3, 2/3)$ , and  $(1/3, 4/3)$  positions are represented by the areas of the circles in the upper part of Figure 9. These peaks correspond to the  $(1,0)_{ad}$ ,  $(2,0)_{ad}$ , and  $(2,1)_{ad}$  peaks from the adlayer lattice, respectively. The  $(1,1)_{ad}$  peak is not included because it overlaps with the  $(1,0)$  substrate peak. Calculations have been performed by using a hollow-site (left panel) and a bridge-site (right panel) model. The coverage and Pb-Br layer spacing in the calculations were fixed at the values obtained from specular reflectivity. The results from the best fit obtained by allowing the in-plane Debye-Waller factor,  $\sigma_{xu}$ , for either Pb or Br to vary, are shown by the sizes of the plus signs. With bromides in the triangular hollow sites of the Pb adlayer, the fit cannot reproduce the main feature that the  $(2,0)_{ad}$  peak is stronger than the  $(1,0)_{ad}$  peak, which rules out this model. An agreement with the measured values has been found by using the model with Br at the bridge site of the Pb adlayer (right panel). The best fit was obtained with  $\sigma_{xu}$  being 0.23 and 0.10 Å for the Pb and Br adlayer, respectively.

Our finding of Br adsorption at the bridge site contradicts prior conclusions on related systems in which the hollow sites are considered more favorable.<sup>8,10</sup> For example, in other published work on the hexagonal CuCl phase, Cl has been proposed to be near the hollow sites of the underlying hexagonal Cu adlayer on the Pt(111) electrode. This proposal is made despite the fact that the observed in-plane intensity pattern is similar to that of PbBr on Au(111) and can be better fitted with Cl at the bridge site.<sup>32</sup> The idea for Cl being near the hollow sites came from the comparison with the 3D zinc blende crystal structure of CuCl. Along the (111) direction of a zinc blende lattice, Cu and Cl form separated hexagonal layers and are in each other's hollow site. Simple sphere packing arguments also favor hollow site because this arrangement provides the maximum number of nearest neighbors. However, the hollow site stacking arrangement in 3D is not necessarily held in 2D for ionic crystals.

In Figure 10 we have evaluated the electrostatic energy of this bilayer configuration as a function of the lateral coordinate  $x$ . Even though image charges of both layers have been included,



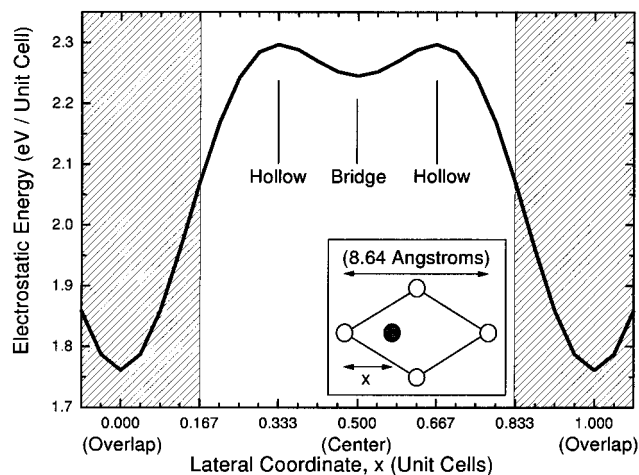


**Figure 10.** Electrostatic energy of two infinite layers of charges with the spacing of the  $(\sqrt{3} \times \sqrt{3})$  lattice of Au(111) (5.00 Å). The layers are situated at 3.00 and 6.15 Å above an ideal sheet of conductor. The shaded regions on the sides are restricted because of the overlap of ionic radii of  $\text{Pb}^{+2}$  and  $\text{Br}^-$ .

the calculation is an example of the classical Madelung problem, so care has been taken with the ordering of terms.

Using a method similar to Evjen,<sup>33</sup> we superimposed a series of charge-neutral concentric shells around a core ion. Unlike Evjen we have always chosen the concentric shells so that ions are never split into halves, thirds, quarters, eighths, etc. For computational purposes, we have located the positive and negative layers at the experimentally found heights of 3.00 and 6.15 Å, respectively, above an assumed plane mirror representing the Au substrate. We have included the image charges of this mirror in all calculations. An atomic spacing of 2.88 Å was used for the Au substrate which determines the lateral spacing of the positive and negative adlayers, each with  $(\sqrt{3} \times \sqrt{3})$  structure.

To reduce the number of computations, we exploited the symmetry of the concentric shells. Mathematica 3.0<sup>34</sup> was programmed to compute the sums. It was observed that the electrostatic energies converge at rates of approximately  $1/r^2$ . Each sum converged typically to at least four significant digits within 2 to 10 min on a contemporary computer. The electrostatic energy at the bridge site was recalculated with two differently shaped concentric shells in addition to the standard shell used at all sites. Also recalculated was the energy at the hollow site with one additional shell shape. All repeated calculations produced consistent results.

We also confirmed our results by removing the image charges, bringing the positive and negative layers into the same plane, and calculating the electrostatic energy at the hollow site. The energy was calculated with the same two sets of concentric shells used at the hollow site in the standard setup. The result was consistent to eight significant digits with a previously published analytical expression for Madelung's constant for the case of our hollow site.<sup>35,36</sup>

Figure 10 displays the electrostatic energy we calculated at various intermediate sites when the image charges were included and the positive and negative layers were set at the experimentally determined heights. Because these positive and negative layers are attractive, the lowest Coulomb energy occurs at  $x = 0$  and  $x = 1$ . This part of the result depends sensitively upon the exact choice of layer positions. However, this region is forbidden because of the quantum mechanical hard-sphere repulsion of the ions which occurs roughly when the separation

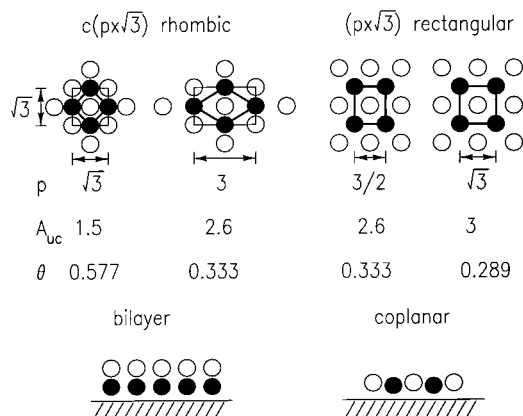


**Figure 11.** In-plane (top) and out-of-plane (bottom) structure models for the  $c(p \times \sqrt{3})$  and  $(p \times \sqrt{3})$  binary ionic adlayers phases on a hexagonally close-packed substrate with certain  $p$  values. The corresponding primitive unit cell areas are calculated in the unit of the substrate lattice constant. The coverage is referred to the atomic density of the substrate and is equal to  $1/p$  and  $1/2p$  for the  $c(p \times \sqrt{3})$  and phases, respectively.

is equal to the sum of the nominal "ionic radii". This overlap region is shaded on the figure. Within the allowed region, it is clear that the bridge configuration,  $x = 0.5$ , is favored over the hollow configuration, with an electrostatic energy advantage of 0.0519 eV per unit cell.

The numerical result for the calculation shown is specific for the problem at hand, but the results that the bridge site is favored over the hollow site is quite general for binary ionic layers, whether the ground-plane (i.e., image charges) is included. The energy in the forbidden regions,  $x = 0$  or  $1$ , is obviously a strong function of the separation of the ionic layers, and even diverges when they overlap exactly. However, the curvature of the energy function near  $x = 0.5$  is generally preserved, and therefore supports the favorability of the bridge site in a wide variety of hexagonal binary ionic systems.

A simple explanation of why the bridge site is favored over the hollow site in a hexagonal (or more generally a rhombic) lattice can be realized by using the ideas discussed in the Introduction and noting that the bridge site is at the center of the rhombic primitive unit cell. For a free-standing 2D crystal with 1:1 stoichiometry, square symmetry should be favored because it allows an ion to surround itself with the maximum number of counterions. As shown in Figure 2, the rectangular and rhombic lattices can be considered as resulting from the substrate influence which causes a distortion from a square to either a rhombus or a rectangle. Our calculation confirmed that, if the ionic interaction is dominant, the counterion should remain at the center for both rectangular and rhombic lattices.

Figure 11 schematically shows four special cases of the  $c(p \times \sqrt{3})$  (in columns I and II) and the  $(p \times \sqrt{3})$  phases (in columns III and IV). All cases apply to a hexagonally packed substrate. A continuum of incommensurate structures exists between columns I and II and also between columns III and IV. The primitive unit cells are outlined by the thick lines, whereas the  $c(p \times \sqrt{3})$  unit cells are outlined by the thin lines. For the  $c(p \times \sqrt{3})$  phase, the area of the primitive unit cell, denoted  $A_{uc}$ , is  $p \times \sqrt{3}/2$ . For the  $(p \times \sqrt{3})$  phase,  $A_{uc}$  is  $p \times \sqrt{3}$ . When  $p = \sqrt{3}$ , both phases (in columns I and IV) have a square primitive unit cell in which the corresponding area of the  $(p \times \sqrt{3})$  is twice that of the  $c(p \times \sqrt{3})$  phase. In the other extreme, columns II and III are the cases for the  $c(3 \times \sqrt{3})$  and  $(3/2 \times \sqrt{3})$ , in which the areas of the primitive unit cells



or the adlayer coverages are the same. These latter two structures are both observed for Pb–Br coadsorption on Au(111). Because both are commensurate and have the same coverage, the driving force for changing the lattice symmetry from rectangular to rhombic at more negative potentials must be the increase of anion–substrate layer spacing caused by the decrease of anion–substrate interaction. As the layer spacing between the cation and anion increases, the coordination number within each adlayer favors an increase from four to six. Reviewing other observed rectangular ( $p \times \sqrt{3}$ ) to rhombic  $c(p \times \sqrt{3})$  phase transitions, we note that the adlayer density also plays a role and the 1/3 coverage seems to be a critical value. The ( $p \times \sqrt{3}$ ) phase has been found with coverage equal to or less than 1/3 (0.333 for TlCl, TlBr, and PbBr; 0.300 for TlI), whereas the coverage of the  $c(p \times \sqrt{3})$  phases for TlCl, TlBr, and PbBr ranges from 0.476 to 0.333. The  $c(p \times \sqrt{3})$  phase is also observed for TlCl and TlBr on Pt(111) with  $p \approx 2.17$ ,<sup>29</sup> corresponding to 0.46 coverage. The symmetry switch-over at 1/3 coverage is likely because the lattice distortion from a square with increasing coverage decreases for the  $c(p \times \sqrt{3})$  phase but increases for the ( $p \times \sqrt{3}$ ) phase near 1/3 monolayer coverage. Because less distortion is preferred, high-coverage adlayers switch to the  $c(p \times \sqrt{3})$  rhombic phase. In all the observed rhombic phases, the anions cannot be in the same plane with the cation because the calculated nearest neighbor spacing within the plane is much smaller than the sum of ionic radii. All these observations suggest that a rhombic lattice is favored for higher density bilayers with respect to the coplanar lower density rectangular phase.

## Summary and Conclusions

In situ SXS studies have been performed for Tl–Cl, Tl–I, and Pb–Br coadsorption on the Au(111) electrode in acid solutions. Similar to Tl–Br/Au(111), a rich structural phase behavior over a wide potential region has been found in these systems. Based on detailed analysis of in-plane diffraction intensity and specular reflectivity, the stoichiometry and the atomic arrangement within the unit cell has been determined unambiguously.

At the most negative potentials, Tl forms a rotated-hexagonal monolayer as it does in the absence of halides. However, the potential region of this pure Tl phase decreases as the anion adsorption strength increases with the order,  $\text{Cl} < \text{Br} < \text{I}$ . Lead also forms a rotated-hexagonal monolayer, but at more positive potentials than Tl. The monolayer lattice is slightly affected by the presence of  $\text{Br}^-$  ion, presumably because of the weak and random adsorption of the bromide anions.

The formation of the 1:1 metal-halide bilayer structures occur near the potential where the hexagonal metal monolayer vanishes. We have shown that not only the  $c(2.10 \times \sqrt{3})$ –TlCl and  $c(2.14 \times \sqrt{3})$ –TlBr, but also the  $(\sqrt{3} \times \sqrt{3})$ –PbBr phase has the counterion at the center of the primitive unit cell. For the  $(\sqrt{3} \times \sqrt{3})$ –PbBr hexagonal phase, this means that the Br ions reside at the bridge site of the underlying hexagonal Pb adlayer, not at the hollow site. Calculation of the electrostatic energy of this bilayer configuration as a function of the lateral coordinate  $x$  shows that the bridge site is favored over the hollow configuration, with an electrostatic energy advantage of 51.9 meV per unit cell.

At more positive potentials, where both metal and anion are adsorbed directly on the substrate surface, 1:1 rectangular lattices are observed. The primitive unit cell is  $(3/2 \times \sqrt{3})$  for TlCl, TlBr, and PbBr, and  $(5/3 \times \sqrt{3})$  for TlI. All the rhombic

phases have a coverage equal to or larger than the 1/3 monolayer. In contrast, the rectangular phases have the coverage equal to or smaller than the 1/3 monolayer. Rhombic symmetry is preferred for higher coverage bilayers over the rectangular coplanar lattices because the coordination number within the cation and anion layers increases from four to six in the transition from a rectangular to a rhombic phase, which is favorable to an increase of lateral density and layer spacing.

For Tl coadsorption with halides, anion-rich phases form at potentials positive with respect to the 1:1 rectangular phases. Not only the 1:2,  $(\sqrt{13} \times \sqrt{13})$ –3TlCl<sub>2</sub>, and  $(\sqrt{13} \times \sqrt{13})$ –3TlBr<sub>2</sub>, but also the 1:3,  $(3 \times 3)$ –TlI<sub>3</sub>, hexagonal structures are found. From analysis of specular reflectivities, anion adsorbates are found in the same layer for  $(\sqrt{13} \times \sqrt{13})$ –TlCl<sub>2</sub> and  $(3 \times 3)$ –TlI<sub>3</sub>, but not for the  $(\sqrt{13} \times \sqrt{13})$ –TlBr<sub>2</sub> phase where half of the Br adsorbates reside in the second layer.<sup>13</sup> This is likely due to the size of Br which is too large for all bromides to be in the same plane. Although different layer spacings are observed, the formation of well-ordered phases appears to be limited to a few stoichiometries that allow high-symmetry arrangements.

The mixed adlayer structures described above can be well understood in terms of 2D ionic crystals with moderate substrate influence. Both metal and anion adsorbates are considered partially charged in well-ordered mixed adlayers because the nearest neighbor spacings determined from the measured lattice constants are close to the sum of ionic radii and the packing symmetries differ distinctly from those of neutral adsorbates. We have proposed that the 1:1 and 1:3 squares and the 1:2 and 1:3 hexagons are the most favorable structures for 2D binary ionic adlayers because of the high degree of symmetry. On hexagonally close-packed substrates, square lattices tend to be distorted to either a rectangle or a rhombus. Nevertheless, the counterion remains at the center of the primitive unit cell. These structural trends are consistent with experimental observations and electrostatic energy calculations.

**Acknowledgment.** We thank B.M. Ocko for useful discussions. This research was performed under the auspices of the US Department of Energy, Divisions of Chemical and Materials Sciences, office of Basic Energy Sciences under Contract DE-AC02-98CH10886. I.K.R. and J.E.D. acknowledge support from Department of Energy under Contract DEFG02-96ER45439.

## Appendix

The measured structure factor intensities of the low-order in-plane diffraction peaks were compared with the predictions based on the proposed structural models. In the calculation,  $q$ -dependent atomic form factors were used, and normalization was made for the strongest peak intensity to have unity value.

For the  $(3 \times \sqrt{3})$ –2TlCl phase, the first three low-order diffractions were used in the analysis. They have  $(1,0)_{\text{ad}}$ ,  $(0,1)_{\text{ad}}$ , and  $(1,1)_{\text{ad}}$  indexes with the primitive adlayer unit cell being the  $(1.5 \times \sqrt{3})$  rectangle. Because the  $(0,2)_{\text{ad}}$  peak from one of the three symmetry equivalent domains overlaps in reciprocal space with the  $(2,1)_{\text{ad}}$  peaks from the other two domains, their intensities were not used in fitting. The measured intensities 0.39, 0.40, and 1.00 for the  $(1,0)_{\text{ad}}$ ,  $(0,1)_{\text{ad}}$ , and  $(1,1)_{\text{ad}}$  peaks were fitted to the  $(3 \times \sqrt{3})$ –2TlCl structure model, and an agreement was obtained with calculated intensities being 0.40, 0.39, and 1.00, respectively. The in-plane Debye–Waller factor,  $\sigma_{xy}$ , for Tl was allowed to vary in the fitting, whereas the coverage and the Tl–Cl layer spacing were fixed to the values

obtained from specular reflectivity analysis and the  $\sigma_{xy}$  for Cl was fixed at the same value as its  $\sigma_z$  (0.1 Å). The best fit was obtained with  $\sigma_{xy}$  for Tl being 0.31 Å, which is close to the  $\sigma_z$  value for Tl (0.35 Å) obtained from fitting specular reflectivity. Because Tl has a larger z-spacing from Au surface than Cl does, the looser bonding may outweigh the larger mass so that the  $\sigma$  values are relatively large for Tl.

For the  $(\sqrt{13} \times \sqrt{13})$ -TlCl<sub>2</sub> hexagonal phase, in-plane diffraction peaks were observed up to the fourth order. The measured intensities, 0.40 for (10), 1.00 for (11), 0.20 for (20), and 0.06 for (21) can be fairly well reproduced (0.42, 1.00, 0.19, and 0.08, respectively) by the calculation based on the  $(\sqrt{13} \times \sqrt{13})$ -TlCl<sub>2</sub> structure model with  $\sigma_{xy}$  for Cl and Tl being 0.1 (fixed) and 0.35 (fitted) Å, respectively.

For the  $(5 \times \sqrt{3})$ -3TII rectangular phase, the measured intensities for both of the (10) and (01) adlayer peaks are 0.06, with the (11) intensity being 1.0. By adjusting the  $\sigma_{xy}$  in the fitting, the measured values were reproduced exactly by the calculation based on the structural model. The odd-order to even-order intensity ratio is smaller for Tl-I than for Tl-Cl in the rectangular phases, because the electron density difference between I and Tl is much smaller than that between Cl and Tl.

## References and Notes

- (1) Toney, M. F.; Gordon, J. G.; Samant, M. G.; Borges, G. L.; Melroy, O. R.; Kau, L. S.; Wiesler, D. G.; Yee, D.; Sorensen, L. B. *Phys. Rev. B* **1990**, *42*, 5594.
- (2) (a) Wang, J. X.; Adžić, R. R.; Ocko, B. M. *J. Phys. Chem.* **1994**, *98*, 7182. (b) Adžić, R. R.; Wang, J. X.; Polewska, W.; Ocko, B. M. *Electrochim. Acta* **1990**, *40*, 83.
- (3) Toney, M. F.; Gordon, J. G.; Samant, M. G.; Borges, G. L.; Melroy, O. R.; Yee, D.; Sorensen, L. B. *J. Phys. Chem.* **1995**, *99*, 4733.
- (4) Wang, J. X.; Adžić, R. R.; Magnussen, O. M.; Ocko, B. M. *Surf. Sci.* **1995**, *335*, 120; **1995**, *344*, 111.
- (5) Manne, S.; Hansma, P. K.; Massie, J.; Elings, V. B.; Gewirth, A. A. *Science* **1991**, *251*, 183.
- (6) Chen, C.-H.; Gewirth, A. A. *J. Am. Chem. Soc.* **1992**, *114*, 5439.
- (7) (a) Magnussen, O. M.; Hotlos, J.; Nichols, R. J.; Kolb, D. M.; Behm, R. J. *Phys. Rev. Lett.* **1990**, *64*, 2929. (b) Magnussen, O. M.; Hotlos, J.; Beitel, G.; Kolb, D. M.; Behm, R. J. *J. Vac. Sci. Technol. B* **1991**, *9*, 969. (c) Sashikata, K.; Furuya, N.; Itaya, K. *J. Electroanal. Chem.* **1991**, *316*, 275. (d) Haiss, W.; Lackey, D.; Sass, J. K.; Meyer, H.; Nichols, R. J. *Chem. Phys. Lett.* **1992**, *200*, 343. (e) Moller, F. A.; Magnussen, O. M.; Behm, R. J. *Phys. Rev. B* **1995**, *51*, 2484. (f) Moller, F.; Magnussen, O. M.; Behm, R. J. *Electrochim. Acta* **1995**, *40*, 1259. (g) Matsumoto, H.; Inukai, J.; Ito, M. *J. Electroanal. Chem.* **1994**, *379*, 223.
- (8) Hotlos, J.; Magnussen, O. M.; Behm, R. J. *Surf. Sci.* **1995**, *335*, 129.
- (9) Toney, M. F.; Howard, J. N.; Richer, J.; Borges, G. L.; Gordon, J. G.; Melroy, O. R.; Yee, D.; Sorensen, L. B. *Phys. Rev. Lett.* **1995**, *75*, 4472.
- (10) (a) Tidswell, I. M.; Lucas, C. A.; Marković, N. M.; Ross, P. N. *Phys. Rev. B* **1995**, *51*, 10205. (b) Lucas, C. A.; Marković, N. M.; Tidswell, I. M.; Ross, P. N. *Physica B* **1996**, *221*, 245.
- (11) (a) Herrero, E.; Glazier, S.; Abruna, H. D. *J. Phys. Chem. B* **1998**, *102*, 9825. (b) Herrero, E.; Glazier, S.; Buller, L. J.; Abruna, H. D. *J. Electroanal. Chem.* **1999**, *461*, 121.
- (12) Adžić, R. R.; Wang, J. X.; Magnussen, O. M.; Ocko, B. M. *J. Phys. Chem.* **1996**, *100*, 14721.
- (13) (a) Wang, J. X.; Robinson, I. K.; Adžić, R. R. *Surf. Sci.* **1998**, *412/413*, 374. (b) Adžić, R. R.; Wang, J. X. *J. Phys. Chem. B* **1998**, *102*, 6305.
- (14) Pauling, L. *The Nature of the Chemical Bond*, 3rd ed.; Cornell University Press: Ithaca, NY, 1960.
- (15) Bridgman, P. W. *Z. Kristallogr.* **1927**, *67*, 363.
- (16) Born, M.; Mayer, J. E. *Z. Phys.* **1932**, *75*, 1.
- (17) Pauling, L. *J. Am. Chem. Soc.* **1928**, *50*, 1036.
- (18) (a) Clavilier, J.; Faure, R.; Guinet, G.; Durand, R. *J. Electroanal. Chem.* **1980**, *107*, 205. (b) Wiechers, J.; Twomey, T.; Kolb, D. M.; Behm, R. J. *J. Electroanal. Chem.* **1988**, *248*, 451.
- (19) Wang, J.; Ocko, B. M.; Davenport, A. J.; Isaacs, H. S. *Phys. Rev. B* **1992**, *46*, 10321.
- (20) (a) Busing, W. R.; Levy, H. A. *Acta Crystallogr.* **1967**, *22*, 457. (b) Mochrie, S. G. J. *J. Appl. Crystallogr.* **1988**, *21*, 1.
- (21) Robinson, I. K. In *Handbook on Synchrotron Radiation*; Moncton, D. E., Brown, G. S., Eds.; North-Holland: Amsterdam, 1991; Vol. 3, p 221.
- (22) The goodness of fit  $\chi^2$  is the sum of squares of the differences between the y-values of the data points and values calculated with the parameters (weighted by 1/y) divided by the degree of freedom (the number of fitted points minus the number of fitted parameters). Hence, the smaller  $\chi^2$  is, the better the fit is.
- (23) Ocko, B. M.; Watson, G. M.; Wang, J. *J. Phys. Chem.* **1994**, *98*, 897.
- (24) (a) Gao, X.; Weaver, M. J. *Phys. Rev. Lett.* **1994**, *73*, 846. (b) Gao, X.; Edens, G. J.; Weaver, M. J. *Phys. Chem.* **1994**, *98*, 8074.
- (25) Emsley, J. *The Elements*, 2nd ed.; Clarendon Press: Oxford, 1991.
- (26) Kittel, C. *Introduction to Solid State Physics*, 5th ed.; John Wiley & Sons, Inc.: New York, 1976.
- (27) Wyckoff, R. *Crystal Structures*, 2nd ed.; Interscience: New York, 1963.
- (28) Wang, J. X.; Waston, G. M.; Ocko, B. M. *J. Phys. Chem.* **1996**, *100*, 6672.
- (29) Unpublished results.
- (30) (a) Herrero, E.; Glazier, S.; Abruna, H. D. *J. Phys. Chem. B* **1998**, *102*, 9825.
- (31) Reniers, F.; Fairbrother, D. H.; Wu, S.; Lipkowski, J. *Surf. Sci.* **1999**, *433*, 12.
- (32) Private communication with Prof. Lucas.
- (33) Evjen, H. *Phys. Rev.* **1932**, *39*, 675.
- (34) *Mathematica 3.0*; Wolfram Research, Inc.: Champaign, IL, 1996.
- (35) Borwein, D.; Borwein, J. M.; Taylor, K. F. *J. Math. Phys.* **1985**, *26*, 2999.
- (36) Zucker, I. J.; Robertson, M. M. *J. Phys. A: Math. Gen.* **1975**, *8*, 874.